

## Breakup process of cylindrical viscous liquid specimens after a strong explosion in the core

B. H. Bang, C. S. Ahn, D. Y. Kim, J. G. Lee, H. M. Kim, J. T. Jeong, W. S. Yoon, S. S. Al-Deyab, J. H. Yoo, S. S. Yoon, and A. L. Yarin

Citation: *Physics of Fluids* **28**, 094105 (2016); doi: 10.1063/1.4962409

View online: <http://dx.doi.org/10.1063/1.4962409>

View Table of Contents: <http://scitation.aip.org/content/aip/journal/pof2/28/9?ver=pdfcov>

Published by the [AIP Publishing](#)

---

### Articles you may be interested in

[Coupling of sausage, kink, and magneto-Rayleigh-Taylor instabilities in a cylindrical liner](#)  
*Phys. Plasmas* **22**, 032706 (2015); 10.1063/1.4915520

[Explosion-driven Rayleigh-Taylor instability in gas-particle mixtures](#)  
*Phys. Fluids* **26**, 043303 (2014); 10.1063/1.4873175

[Hydrodynamic analysis of laser-driven cylindrical implosions](#)  
*Phys. Plasmas* **20**, 082705 (2013); 10.1063/1.4818801

[Development of two mix model postprocessors for the investigation of shell mix in indirect drive implosion cores](#)  
*Phys. Plasmas* **14**, 072705 (2007); 10.1063/1.2753471

[Rayleigh-Taylor and Richtmyer-Meshkov instabilities and mixing in stratified cylindrical shells](#)  
*Phys. Fluids* **17**, 094105 (2005); 10.1063/1.2046712

---

An advertisement for Physics Today featuring a magnifying glass icon over the text 'Looking for a specific instrument?'. Below this, it says 'Easy access to the latest equipment. Shop the Physics Today Buyer's Guide.' To the right, there is a list of equipment categories: 'lasers', 'imaging', 'VACUUM EQUIPMENT', 'instrumentation', 'software', 'cryogenics', and 'MATERIALS' in large blue letters, followed by '+ MORE...'. The 'PHYSICS TODAY' logo is in the top right corner.

Looking for a specific instrument?

Easy access to the latest equipment.  
Shop the *Physics Today* Buyer's Guide.

PHYSICS TODAY

lasers imaging  
VACUUM EQUIPMENT  
instrumentation  
software MATERIALS  
cryogenics + MORE...

## Breakup process of cylindrical viscous liquid specimens after a strong explosion in the core

B. H. Bang,<sup>1,2</sup> C. S. Ahn,<sup>1,3</sup> D. Y. Kim,<sup>1</sup> J. G. Lee,<sup>1</sup> H. M. Kim,<sup>4</sup> J. T. Jeong,<sup>4</sup> W. S. Yoon,<sup>4</sup> S. S. Al-Deyab,<sup>5</sup> J. H. Yoo,<sup>6</sup> S. S. Yoon,<sup>1,a)</sup> and A. L. Yarin<sup>7,a)</sup>

<sup>1</sup>School of Mechanical Engineering, Korea University, Seoul 136-713, South Korea

<sup>2</sup>Plant and Environmental Research Team, Daewoo Institute of Construction Technology, 60, Songjuk-dong, Jangan-gu, 440-210 Suwon, South Korea

<sup>3</sup>Fire Research Center, Korea Institute of Construction Technology, 283, Goyang-daero, Ilsanseo-gu 10223, Goyang-si, South Korea

<sup>4</sup>School of Mechanical Engineering, Yonsei University, Seoul 120-752, South Korea

<sup>5</sup>Petrochemical Research Chair, Department of Chemistry, King Saud University, Riyadh 11451, Saudi Arabia

<sup>6</sup>Agency for Defense Development, P.O. Box 35 Yuseong, Daejeon, South Korea

<sup>7</sup>Department of Mechanical & Industrial Engineering, University of Illinois at Chicago, 842 W. Taylor St., Chicago, Illinois 60607, USA

(Received 8 July 2016; accepted 26 August 2016; published online 30 September 2016)

Basic understanding and theoretical description of the expansion and breakup of cylindrical specimens of Newtonian viscous liquid after an explosion of an explosive material in the core are aimed in this work along with the experimental investigation of the discovered phenomena. The unperturbed motion is considered first, and then supplemented by the perturbation growth pattern in the linear approximation. It is shown that a special non-trivial case of the Rayleigh-Taylor instability sets in being triggered by the gas pressure differential between the inner and outer surfaces of the specimens. The spectrum of the growing perturbation waves is established, as well as the growth rate found, and the debris sizes evaluated. An experimental study is undertaken and both the numerical and analytical solutions developed are compared with the experimental data. A good agreement between the theory and experiment is revealed. It is shown that the debris size  $\lambda$ , the parameter most important practically, scales with the explosion energy  $E$  as  $\lambda \sim E^{-1/2}$ . Another practically important parameter, the number of fingers  $N$  measured in the experiments was within 6%-9% from the values predicted numerically. Moreover,  $N$  in the experiments and numerical predictions followed the scaling law predicted theoretically,  $N \sim m_e^{1/2}$ , with  $m_e$  being the explosive mass. *Published by AIP Publishing.* [<http://dx.doi.org/10.1063/1.4962409>]

### I. INTRODUCTION

Theoretical and experimental studies of the accelerated motions of viscous planar and viscoelastic cylindrical liquid specimens under the action of a gas pressure differential between the free surfaces revealed that these flows with free surfaces are prone to a special non-trivial type of the Rayleigh-Taylor instability, which governs their breakup through a concerted internal mechanism and determines the debris size.<sup>1</sup> The main focus of that work was in the electrical explosions of tungsten wires at the axes of viscoelastic cylindrical specimens, which were tackled experimentally, albeit some other types of rheological behavior of liquids, and the other types of explosions, e.g., the underwater nuclear explosions were explored.<sup>2,3</sup> The results of these works are covered in Chap. 5 in the following monograph.<sup>4</sup>

<sup>a)</sup> Authors to whom correspondence should be addressed. Electronic addresses: [ayarin@uic.edu](mailto:ayarin@uic.edu) and [skyoona@korea.ac.kr](mailto:skyoona@korea.ac.kr)

Currently FAE (Fuel-Air-Explosive) bombs are in focus. FAE is a thermobaric weapon comprised of slurry (i.e., liquid fuel and aluminum particles) and uses surrounding air as an oxidizer. Because of the absence of an oxidizer inside the bomb, it contains greater explosive power per mass of warheads whose light payload is beneficial for delivery either on ground or in air. The slurry consistence of the bomb facilitates enhancement of fuel dispersion and subsequent detonation, as compared to the one which contains only aluminum particles without fuel.<sup>5,6</sup> However, the physical mechanism of the fuel dispersion in such cases has not been fully understood yet. In particular, the growth of the interfacial waves on the exploding liquid in contact with the surrounding air, the process known as the first “near-field” phase after which the second “far-field” phase arises, is not understood well. At the first phase, the primary breakup occurs after the unstable waves (ligaments or fingers) form droplets. At the second phase, the primary droplets again breakup into smaller droplets due to the aerodynamic drag, which is called the secondary breakup. These primary and secondary breakup processes are the main subject of the current FAE research.

Numerical and analytical models for the first breakup phase were provided in Ref. 7. However, the analytical model was limited to an ideal 1D potential flow. The effect of viscosity was taken into consideration in Ref. 8, albeit the model was limited to 1D cases. In Ref. 9, the breakup of a liquid sheet in the presence of shock waves was predicted. In Ref. 10, slurry dispersion and cavitation induced by the shock wave in explosion was modeled and verified by measuring the dispersion of aluminum and SiO<sub>2</sub> particles. In Ref. 11, the experimental data for the expanding radius as a function of time for various explosive scenarios were provided, as well as a simple model describing the data was proposed. Visualization of the liquid dispersion process by explosion in an X-ray equipment was conducted in Ref. 12. Liquid dispersion due to FAE explosion was visualized in Ref. 13. In Ref. 14, it was emphasized that all the preceding studies lack consideration of the Rayleigh-Taylor instability, which takes place during rapid acceleration of liquid toward the surrounding air and is the leading physical mechanism of the phenomena under consideration. The latter is the main goal of the present work. It should be emphasized that the free surface flows generated by strong explosions inside liquid specimens have nothing in common with the classical strong explosion case studied in gas dynamics.<sup>15–19</sup>

In the present work, the case of cylindrical specimens of Newtonian viscous liquids with surface tension, which evolve under the action of the explosion of a concentric explosive in the core, is considered as depicted in Fig. 1. The explosion process and the resulting gas pressure in the cavity

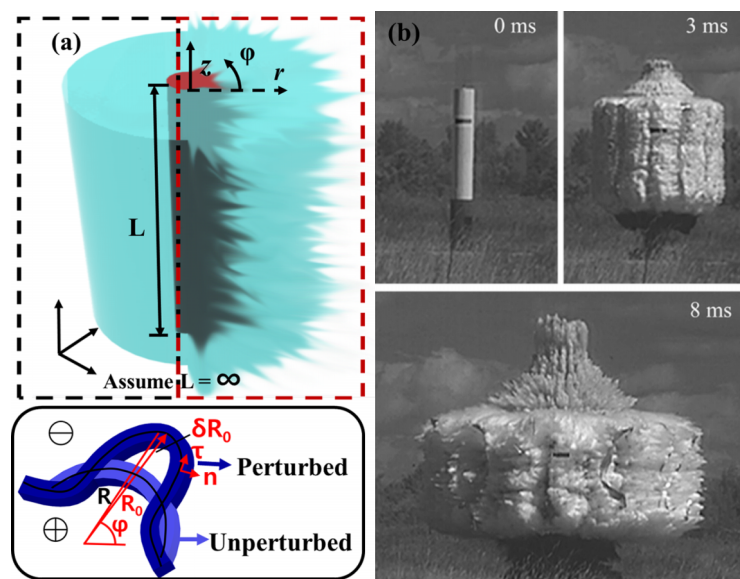


FIG. 1. (a) Sketch of a cylindrical specimen expanding after an explosion in the core. On the left is an imaginary unperturbed case, while on the right is the perturbed case. (b) Experimental observations, the growing perturbations are clearly visible. Reprinted with permission from F. Zhang *et al.*, *Shock Waves* **25**, 239–254 (2015). Copyright 2015 Springer.

are described in Section II. The unperturbed radial motion of liquid is described in Section III. The perturbed motion is covered in Section IV. The rheological constitutive equation of viscous Newtonian fluids is used in Section V to find the deviatoric viscous stresses, which allows problem formulation in the closed form, as in Section VI. The spectrum of the growing perturbations of the problem with the “frozen” coefficients corresponding to the very beginning of the motion is found in Section VII. There the physical nature of the instability is attributed to the special case of the Rayleigh-Taylor mechanism driven by the acceleration of liquid toward the outside gas under the action of a pressure differential resulting from the explosion. The governing equations used for the numerical simulations of the general (“unfrozen”) case are listed in Section VIII. The analytic solution is compared with the numerical solution in Section IX. Section X is devoted to the experimental investigation. In this section, the experimental data are presented and compared with the numerical solution for validation. The conclusions are drawn in Section XI.

## II. EXPLOSION IN THE SPECIMEN CORE

Assume that a cylindrical explosive goes off instantaneously in the core of a cylindrical specimen. Both the explosive and the specimen are assumed to be long enough to neglect the effect of the axial ( $z$ ) direction and consider the problem in polar coordinates (the radial and the azimuthal coordinates, with the latter being denoted by  $\varphi$ ) as depicted in Fig. 1.

The explosive practically instantaneously (on the scale of  $1 \mu\text{s}$ , Ref. 20, which is much shorter than the characteristic time of the instability in the experiments, which is of the order of 1 ms-cf. Figs. 11 and 12 below) turns into gas, i.e., the mixture of the detonation products, with the internal energy  $E$ . The latter is fully determined by the explosive type and is known. Accordingly,

$$E = \frac{M}{\mu_a} c_v T_0, \quad (1)$$

where  $M$  is the total gas mass,  $\mu_a$  is the atomic mass of the gas,  $c_v$  is its specific heat at constant volume (the molar heat capacity), and  $T_0$  is the initial gas temperature.

The gas pressure in the cavity is higher than the one outside the specimen. Therefore, the accelerated specimen expansion begins. In the first approximation, it is assumed that the gas expansion inside the cavity is adiabatic and thus the gas pressure in the cavity  $P_0^+$  is related to its density  $\rho_g$  as

$$P_0^+ = P_{00}^+ \left( \frac{\rho_g}{\rho_{g0}} \right)^\gamma, \quad (2)$$

where  $\gamma$  is the adiabatic index of the gaseous explosion products, and  $P_{00}^+$  and  $\rho_{g0}$  denote the initial values of the pressure in the cavity and the gas density. It should be emphasized that given the size of the cavity of about  $10^{-1}$ -1 cm, and the speed of sound in the gaseous explosion products, which is at least 340 m/s, it takes about  $10^{-5}$  s for the gas pressure in the cavity to be equilibrated, which is significantly shorter than the characteristic time of the instability in the experiments (about 1 ms, as per Figs. 11 and 12 below). Therefore, the assumption of a uniform gas pressure in the cavity is fully justified.

If one assumes an unperturbed cylindrical expansion of a specimen, the shape of its central line is being described by radius  $R_0(t)$ , where  $t$  is time (see Fig. 1(a), left). Then, due to the mass conservation of the gas in the cavity,

$$\frac{\rho_g}{\rho_{g0}} = \left( \frac{R_{00}}{R_0} \right)^2 \quad (3)$$

with  $R_{00}$  being the initial value of  $R_0(t)$  at  $t = 0$ .

Denote the initial unperturbed radial thickness of the specimen as  $H_0$ . Then, the liquid mass per unit axis length  $m$  is given by

$$m = \rho 2\pi R_{00} H_0 \times 1 \quad (4)$$

with  $\rho$  being liquid density.

Accordingly, the expansion velocity scale  $v_0$  is defined as

$$v_0 = \sqrt{2 \frac{E}{m}} = \sqrt{\frac{E_1}{\rho \pi R_{00} H_0}}, \quad (5)$$

where  $E_1$  is the explosive energy released per unit specimen length, having the unit of J/m.

As the length scale it is appropriate to use  $R_{00}$ . Then, combining Eqs. (2) and (3), one obtains

$$P_0^+ = \frac{P_{00}^+}{r^{2\gamma}} \quad (6)$$

with  $r = r(t) = R_0(t)/R_{00}$  being the dimensionless unperturbed radius of the centerline.

It should be emphasized that the domain filled with liquid is characterized not only by its centerline but also by its thickness (cf. Fig. 1; both the centerline and the thickness can vary in the azimuthal direction). Both geometric characteristics are linked via the liquid mass conservation when the liquid domain stays intact (albeit possibly perturbed), and the theory outlined in Sections III–XI describes them simultaneously. Therefore, there should be no confusion: when only the centerline is mentioned, the non-zero thickness is automatically implied.

### III. UNPERTURBED LIQUID MOTION

The liquid motion is described in the framework of the quasi-two-dimensional equations of liquid films,<sup>4</sup> which in the present case are reduced to the quasi-one-dimensional equations because there is no dependence on the axial coordinate. Accordingly, the unperturbed motion is described by the following equations:

The kinematic equation,

$$\frac{dR_0}{dt} = V_0 \quad (7)$$

with  $V_0$  being the unperturbed radial velocity of the centerline.

The mass balance (the continuity) equation,

$$h_0 = \frac{H_0 R_{00}}{R_0} \quad (8)$$

with  $h_0$  being the current radial thickness of the liquid specimen. This is an example of the automatic link between the centerline radius (unperturbed in the present case) and the specimen thickness (also, unperturbed in this case).

The momentum balance equation,

$$\frac{dV_0}{dt} = \frac{\Delta P_0}{\rho h_0} - \frac{\tau_0}{\rho R_0} - \frac{2\alpha}{\rho h_0 R_0}, \quad (9)$$

where the pressure differential between the inner and outer specimen surfaces  $\Delta P_0 = P_0^+ - P_0^-$ , with  $P_0^-$  being the outside pressure, which is constant and known (either being the atmospheric pressure, or vacuum; in the latter case,  $P_0^- = 0$ ). Also,  $\tau_0 = \tau_{11}^0 - \tau_{33}^0$ , where  $\tau_{11}^0$  is the unperturbed deviatoric azimuthal viscous stress, and  $\tau_{33}^0$  is the unperturbed deviatoric radial viscous stress. In addition,  $\alpha$  is the surface tension coefficient.

It is emphasized that the unperturbed radial acceleration of the liquid specimen wall  $A_0 = dV_0/dt$  is determined by the positive pressure differential  $\Delta P_0$ , while the viscous stresses  $\tau_0 > 0$  and surface tension [the last term on the right in Eq. (9)] are counteracting. In the cases of interest,  $A_0$  is always positive, i.e., the liquid motion is radially accelerated toward the outside gas (or vacuum).

### IV. PERTURBED LIQUID MOTION

In any system, perturbations are always present from the very beginning. Normally they are initially very small. For example, in the present case, perturbations are introduced at the very beginning as small imperfections of the explosive or specimen shape, etc. If a system is stable, small

perturbations will fade in the course of motion. On the other hand, in an unstable system (as will be in the present case), small perturbations will grow and eventually disrupt the basic flow. Still, at the initial stage of growth, perturbations are small. Then, the equations of motion detailed in Ref. 4 (see below) can be linearized accounting for their small amplitudes, and the linear equations of the perturbed motion can be solved on the background of the unperturbed motion described by the equations of Section III. Namely, the equations of the unperturbed motion (7)–(9) stay unaffected by the perturbed motion, while the latter is affected by solutions of Eqs. (7)–(9). Such partially conjugate problem of the perturbed motion can be solved very effectively in the framework of the linear stability analysis and elucidate the question whether the system is unstable, and if yes, what are the growing perturbation modes and what is the corresponding rate of perturbation growth.

Introduce the dimensionless small bending perturbations of the centerline of a liquid specimen  $\delta(t, \varphi)$  as (see Fig. 1(a)); with the dimensional perturbation  $\delta R_0 = R_0 \delta$

$$R(t, \varphi) = R_0(t)[1 + \delta(t, \varphi)], \quad (10)$$

where  $R(t, \varphi)$  is the perturbed position of the centerline and  $\delta \ll 1$ .

Similarly, the dimensionless small perturbations of the specimen thickness  $\chi(t, \varphi)$  are introduced as

$$h(t, \varphi) = h_0(t)[1 + \chi(t, \varphi)], \quad (11)$$

where  $h(t, \varphi)$  is the perturbed thickness and  $\chi \ll 1$ . The centerline perturbation  $\delta$  and the perturbation of the specimen thickness  $\chi$  are related by the balance equations described below, as their unperturbed counterparts considered above.

Note also, that the unperturbed motion of Eqs. (7)–(9) is perfectly radial, and there is no flow component in the direction of the centerline. However, in the perturbed case, such a flow component will appear. It is denoted as  $\omega(t, \varphi)$  and  $\omega \ll 1$ .

Using the equations of motion of Ref. 4 and separating the small perturbations from the unperturbed flow via linearization, we arrive at the following system of linear equations for the perturbations:

The linearized perturbed continuity equation

$$\frac{\partial \chi}{\partial t} = \frac{\partial \delta}{\partial t} + \frac{\partial \omega}{R_0 \partial \varphi} = 0. \quad (12)$$

The linearized perturbed momentum balance equation projected onto the centerline

$$\frac{\partial \omega}{\partial t} + \omega \frac{V_0}{R_0} + A_0 \frac{\partial \delta}{\partial \varphi} = \frac{1}{\rho R_0} \frac{\partial \tau'}{\partial \varphi} + \frac{\tau_0}{\rho R_0} \frac{\partial \chi}{\partial \varphi} + \frac{\alpha h_0}{2\rho R_0^3} \left[ 2 \frac{\partial \chi}{\partial \varphi} + \frac{\partial^3 \chi}{\partial \varphi^3} - 2 \left( \frac{\partial \delta}{\partial \varphi} + \frac{\partial^3 \delta}{\partial \varphi^3} \right) \right]. \quad (13)$$

The linearized perturbed momentum balance equation projected onto the normal to the centerline

$$\frac{\partial^2 \delta}{\partial t^2} + \frac{2V_0}{R_0} \frac{\partial \delta}{\partial t} + \frac{2A_0}{R_0} \delta + \frac{A_0}{R_0} \chi = \frac{\Delta P_0}{\rho h_0 R_0} \delta + \left( \frac{\tau_0}{\rho R_0^2} + \frac{2\alpha}{\rho h_0 R_0^2} \right) \frac{\partial^2 \delta}{\partial \varphi^2} - \frac{\tau_0}{\rho R_0^2} \chi - \frac{\tau'}{\rho R_0^2}. \quad (14)$$

In Eqs. (13) and (14),  $\tau' = \tau_{11}' - \tau_{33}'$ , where  $\tau_{11}'$  is the perturbed deviatoric viscous stress in the centerline direction, and  $\tau_{33}'$  is the perturbed deviatoric viscous stress in the direction normal to the centerline.

It should be emphasized that in comparison with the corresponding Section VIII of Chap. 5 in Ref. 4, in Eqs. (13) and (14), the pressure perturbations in the surrounding gas (inside the specimen cavity and outside the specimen) are neglected, since their effect is not expected to be very significant. On the other hand, Eqs. (13) and (14) account for the effect of the surface tension, since in the present case of Newtonian liquid, stabilization of the short wavelengths is possible only by surface tension, in distinction from the case of the elastic liquid treated in Section VIII of Chap. 5 in Ref. 4. Such a regularization of the short wavelengths is a formal requirement for the well-posedness of any perturbation problem and is dictated by the physics of the present problem.

The system of Eqs. (12)–(14) is linear relative to the unknowns  $\chi$ ,  $\omega$ , and  $\delta$ . However, it contains the coefficients determined by the unperturbed flow via Eqs. (7)–(9), namely,  $R_0(t)$ ,  $V_0(t)$ , and

$A_0(t)$ , which shows that its solution in general cannot depend on time exponentially, as in the cases with constant coefficients stemming from the time-independent basic flows.

**V. RHEOLOGICAL CONSTITUTIVE EQUATION OF VISCOUS NEWTONIAN FLUIDS AND DEVIATORIC VISCOUS STRESSES**

The Newton-Stokes rheological constitutive equation assumes a linear dependence between the deviatoric stress tensor  $\boldsymbol{\tau}_s$  and the rate-of-stress tensor  $\mathbf{D} = (\nabla\mathbf{v} + \nabla\mathbf{v}^T)/2$ , with  $\nabla\mathbf{v}$  being the tensor gradient of velocity. Namely, for the incompressible liquids, it is assumed that

$$\boldsymbol{\tau}_s = 2\mu\mathbf{D}, \tag{15}$$

where  $\mu$  is the viscosity.

In the present quasi-one-dimensional case, it is possible to show that

$$\mathbf{D} = \boldsymbol{\tau}\boldsymbol{\tau} \left( \frac{V_0}{R_0} + \frac{\partial\delta}{\partial t} + \frac{\partial\omega}{R_0\partial\varphi} \right) - \mathbf{nn} \left( \frac{V_0}{R_0} - \frac{\partial\chi}{\partial t} \right). \tag{16}$$

Here the dyadic product  $\boldsymbol{\tau}\boldsymbol{\tau}$  of the unit tangent vectors to the centerline  $\boldsymbol{\tau}$  corresponds to the 1-1 direction, while the dyadic product  $\mathbf{nn}$  of the unit normal vectors to the centerline  $\mathbf{n}$  corresponds to the 3-3 direction. Therefore, one finds from Eqs. (15) and (16)

$$\tau_{11}^0 = 2\mu \frac{V_0}{R_0}, \quad \tau_{33}^0 = -2\mu \frac{V_0}{R_0}, \tag{17}$$

$$\tau'_{11} = 2\mu \left( \frac{\partial\delta}{\partial t} + \frac{\partial\omega}{R_0\partial\varphi} \right), \quad \tau'_{33} = 2\mu \frac{\partial\chi}{\partial t}. \tag{18}$$

Hence,

$$\tau_0 = 4\mu \frac{V_0}{R_0}, \quad \tau' = 2\mu \left( \frac{\partial\delta}{\partial t} + \frac{\partial\omega}{R_0\partial\varphi} - \frac{\partial\chi}{\partial t} \right). \tag{19}$$

**VI. COMPLETE SET OF GOVERNING EQUATIONS IN THE DIMENSIONLESS FORM**

Combining the unperturbed Eqs. (7)–(9) with the perturbed Eqs. (12)–(14), substituting the rheological Eq. (19), and making use of Eq. (6), one arrives at the following system of the dimensionless equations:

$$\frac{dr}{d\tau} = u, \tag{20}$$

$$\frac{du}{d\tau} = \frac{(\gamma - 1)}{r^{2\gamma-1}} - \frac{2P_2r}{Q} - \frac{4}{\text{Re}} \frac{u}{r^2} - \frac{2}{r\text{We}}, \tag{21}$$

$$\frac{\partial\chi}{\partial\tau} + \frac{\partial\delta}{\partial\tau} + \frac{\partial\omega_1}{r\partial\varphi} = 0, \tag{22}$$

$$\begin{aligned} \frac{\partial\omega_1}{\partial\tau} + \omega_1 \frac{u}{r} + a \frac{\partial\delta}{\partial\varphi} &= \frac{2}{\text{Re}} \frac{1}{r} \left( \frac{\partial^2\delta}{\partial\tau\partial\varphi} + \frac{1}{r} \frac{\partial^2\omega_1}{\partial\varphi^2} - \frac{\partial^2\chi}{\partial\tau\partial\varphi} \right) \\ &+ \frac{4}{\text{Re}} \frac{u}{r^2} \frac{\partial\chi}{\partial\varphi} + \frac{1}{\text{We}} \frac{Q^2}{8r^4} \left[ 2 \frac{\partial\chi}{\partial\varphi} + \frac{\partial^3\chi}{\partial\varphi^3} - 2 \left( \frac{\partial\delta}{\partial\varphi} + \frac{\partial^3\delta}{\partial\varphi^3} \right) \right], \end{aligned} \tag{23}$$

$$\begin{aligned} \frac{\partial^2\delta}{\partial\tau^2} + \frac{2u}{r} \frac{\partial\delta}{\partial\tau} + \frac{2a}{r} \delta + \frac{a}{r} \chi &= \left[ \frac{(\gamma - 1)}{r^{2\gamma}} - \frac{2P_2}{Q} \right] \delta \\ &+ \left( \frac{4}{\text{Re}} \frac{u}{r^3} + \frac{2}{\text{We}} \frac{1}{r^2} \right) \frac{\partial^2\delta}{\partial\varphi^2} - \frac{4}{\text{Re}} \frac{u}{r^3} \chi - \frac{2}{\text{Re}} \frac{1}{r^2} \left( \frac{\partial\delta}{\partial\tau} + \frac{1}{r} \frac{\partial\omega_1}{\partial\varphi} - \frac{\partial\chi}{\partial\tau} \right). \end{aligned} \tag{24}$$

The dimensionless unperturbed radius, velocity, time, and acceleration  $r$ ,  $u$ ,  $\tau$  and  $a$ , respectively, as well as the dimensionless azimuthal velocity perturbation  $\omega_1$  in Eqs. (20)–(24), are

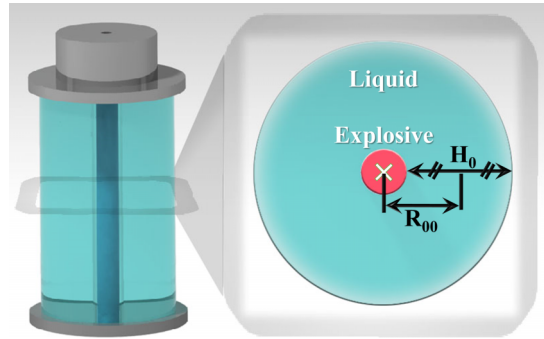


FIG. 2. The initial arrangement of the explosive inside the cylindrical liquid specimen.

introduced according to the following expressions:

$$r = \frac{R_0}{R_{00}}, \quad u = \frac{V_0}{v_0}, \quad \tau = \frac{tv_0}{R_{00}}, \quad a = \frac{du}{d\tau} = \frac{A_0 R_{00}}{v_0^2}, \quad \omega_1 = \frac{\omega}{v_0}. \quad (25)$$

In addition, the following dimensionless groups appear:

$$Re = \frac{\rho v_0 R_{00}}{\mu}, \quad We = \frac{\rho H_0 v_0^2}{\alpha}, \quad Q = \frac{2H_0}{R_{00}}, \quad P_2 = \frac{P_0^-}{\rho v_0^2}, \quad (26)$$

where  $Re$  and  $We$  are the Reynolds and Weber numbers, respectively.

The dimensionless group,  $Q = 2H_0/R_{00}$ , characterizing the initial geometry of the specimen is illustrated by the sketch in Fig. 2. If the explosive rod in the middle becomes wider, the parameter  $Q$  reduces. If the rod surface approaches the outer radius of the specimen, the thickness of the latter  $H_0$  tends to zero and so is  $Q$ . On the contrary, if the explosive rod becomes infinitesimally small (a very thin wire), then  $H_0 = 2R_{00}$  and thus  $Q = 4$ . Accordingly, the range of  $Q$  is  $0 < Q < 4$ .

## VII. SPECTRUM OF GROWING PERTURBATIONS RIGHT AFTER THE EXPLOSION: THE STABILITY PROBLEM WITH THE “FROZEN” COEFFICIENTS

The stability problem describing the evolution of small dimensionless perturbations of the specimen thickness, the azimuthal velocity, and the bending amplitude  $\chi$ ,  $\omega_1$  and  $\delta$ , respectively, given by Eqs. (22)–(24) involves time-dependent coefficients  $r(\tau)$ ,  $u(\tau)$ , and  $a(\tau)$ , determined by the unperturbed part of the problem, Eqs. (20) and (21). This partially conjugate stability problem will be tackled in Sec. VIII. However, an insight into the nature of the instability, as well as its initial moments, can be achieved considering the basic flow to be “frozen,” i.e., assuming that the time-dependent coefficients in Eqs. (22)–(24) are “frozen” at their initial values

$$r \equiv 1, \quad u \equiv 0, \quad a = a_0 = (\gamma - 1) - \frac{2P_2}{Q} - \frac{2}{We}. \quad (27)$$

It should be emphasized that only in the cases where  $a_0 > 0$ , an accelerated expansion of the inner cavity is possible, and only such cases are considered here and hereinafter.

The stability problem with constant coefficients obviously admits the exponential solutions of the following type:

$$\chi = \chi_0 \exp(\nu\tau + is\varphi), \quad \omega_1 = \omega_{10} \exp(\nu\tau + is\varphi), \quad \delta = \delta_0 \exp(\nu\tau + is\varphi), \quad (28)$$

where  $\chi_0$ ,  $\omega_{10}$ , and  $\delta_0$  are the amplitudes of the initial perturbations,  $i$  is the imaginary unit, and  $s$  is the azimuthal wavenumber, which can be positive integers. The unknown perturbation growth rate (increment) is denoted by  $\nu$ .

Substituting Eqs. (27) and (28) into Eqs. (22)–(24), one finds that the problem has non-trivial solutions only when the increment satisfies the following characteristic equation which determines

the spectrum of the problem  $v = v(s)$ :

$$\begin{aligned}
 v^4 + v^3 \frac{4}{\text{Re}} (1 + s^2) + v^2 \left[ -\frac{Q^2 s^2 (2 - s^2)}{8\text{We}} - \frac{2(1 - s^2)}{\text{We}} \right] \\
 + v \left[ -\frac{Q^2 s^2 (2 - s^2)}{2\text{WeRe}} - \frac{8s^2 (1 - s^2)}{\text{WeRe}} + \frac{8s^2 a_0}{\text{Re}} - \frac{Q^2 s^2 (-4 + 3s^2)}{2\text{WeRe}} \right] \\
 + \left[ -a_0^2 s^2 + \frac{Q^2 s^2 a_0 (-4 + 3s^2)}{8\text{We}} + \frac{Q^2 s^2 (2 - s^2) (1 - s^2)}{4\text{We}^2} \right] = 0.
 \end{aligned} \tag{29}$$

This is the 4th order algebraic equation for  $v$ . Before addressing its solutions in the general case, let us consider its important particular cases first.

The first important particular case is the case of an inviscid liquid without surface tension where  $\text{Re} = \text{We} = \infty$ . Then, Eq. (29) reduces to

$$v^4 - a_0^2 s^2 = 0. \tag{30}$$

Among its four roots, there is one real positive root

$$v = \sqrt{a_0 s}. \tag{31}$$

This root means that the problem is unstable and the perturbation amplitudes in Eq. (28) exponentially increase in time. The solution (31) corresponds to the special non-trivial case of the Rayleigh-Taylor instability driven by the gas pressure differential accelerating liquid layer toward the outside atmosphere or vacuum.<sup>4</sup> It is emphasized that in the absence of the surface tension, the situation is ill-posed, and the short-wavelength perturbations corresponding to large wavenumbers  $s$  rapidly and unrestrictedly grow, i.e.,  $v \rightarrow \infty$  as  $s \rightarrow \infty$ . Only surface tension or liquid elasticity could prevent that by introducing regularization of the short wavelengths.

Another particular case of interest is that of viscous Newtonian liquid without surface tension, i.e., now only  $\text{We} = \infty$ . Then, Eq. (29) reduces to

$$v^4 + v^3 \frac{4}{\text{Re}} (1 + s^2) + v \frac{8s^2 a_0}{\text{Re}} - a_0^2 s^2 = 0. \tag{32}$$

In this equation, starting from the left-hand side, three coefficients of the polynomial are positive, while the next one (the 4th,  $-a_0^2 s^2$ ) is negative. Therefore, the coefficient signs change only once and according to Descartes's rule of signs,<sup>21</sup> Eq. (32) has a single real positive root. This root is obviously responsible for the Rayleigh-Taylor instability, albeit amended by the damping viscous effects, but still ill-posed in the absence of surface tension.

The third particular case of interest is the case of an inviscid liquid with non-zero surface tension, i.e., now only  $\text{Re} = \infty$ . Then, Eq. (29) reduces to

$$v^4 - v^2 \left[ \frac{Q^2 s^2 (2 - s^2)}{8\text{We}} + \frac{2(1 - s^2)}{\text{We}} \right] + \left[ -a_0^2 s^2 + \frac{Q^2 s^2 a_0 (-4 + 3s^2)}{8\text{We}} + \frac{Q^2 s^2 (2 - s^2) (1 - s^2)}{4\text{We}^2} \right] = 0.
 \tag{33}$$

The case of  $s = 0$  is of no interest, since there are no azimuthal waves then. The case of  $s = 1$  is also of no interest, since it corresponds to a shift of a circular cross section as a whole. Therefore, only the cases with  $s \geq 2$  should be considered in the present section. Then, in Eq. (33), the first coefficient of the polynomial on the left is positive, while the second one is negative. The third coefficient  $[-a_0^2 s^2 + Q^2 s^2 a_0 (-4 + 3s^2)/(8\text{We}) + Q^2 s^2 (2 - s^2) (1 - s^2)/(4\text{We}^2)]$  contains the first negative term and two subsequent positive terms. If the latter two terms will dominate (at large  $s$  and finite  $\text{We}$ ), the third coefficient will be positive and there will be two sign changes in the coefficients of Eq. (33). Then, according to Descartes's rule of signs, there will be no positive roots, and the problem will be stable. Only if the third coefficient in Eq. (33) will be negative (at smaller  $s \geq 2$  and large enough  $\text{We}$ ), there will be only one change of sign in the coefficients in Eq. (33), and thus, according to Descartes's rule of signs, there will be one positive root and the Rayleigh-Taylor instability. This shows that the finite Weber number (the non-zero surface tension) regularizes the

behavior of the short wavelengths, which are always stable, while the instability sets in within the domain of the longer wavelengths (at smaller  $s \geq 2$ ). The detailed analysis shows that the third coefficient in Eq. (33) changes sign at  $s_1 = \sqrt{2a_0We/Q}$ , i.e., the short wavelengths corresponding to wavenumbers

$$s_1 > \sqrt{\frac{2a_0We}{Q}} \tag{34}$$

are stabilized by the surface tension.

Consider now the entire characteristic equation (29). Starting from the left-hand side, at  $s \geq 2$ , the first three terms are positive. The fourth one

$$-\frac{Q^2s^2(2-s^2)}{2WeRe} - \frac{8s^2(1-s^2)}{WeRe} + \frac{8s^2a_0}{Re} - \frac{Q^2s^2(-4+3s^2)}{2WeRe} = \frac{8s^2a_0}{Re} - (1-s^2)\frac{(16s^2-2Q^2s^2)}{2ReWe} \tag{35}$$

is also positive at  $s \geq 2$ , since only cases with  $Q^2 < 1$  are of interest.

Then, only the fifth term on the left in Eq. (29), which is  $[-a_0^2s^2 + Q^2s^2a_0(-4 + 3s^2)/(8We) + Q^2s^2(2 - s^2)(1 - s^2)/(4We^2)]$  can be negative at

$$2 \leq s < s_1 = \sqrt{\frac{2a_0We}{Q}}. \tag{36}$$

Then, in this band, there is a single positive root of Eq. (29), and the Rayleigh-Taylor instability sets in. Otherwise, the short wavelengths with the large wavenumbers of the inequality (34) will be stabilized by the surface tension.

Note that the dimensionless cut-off wavenumber  $s_1$  corresponds to the azimuthal cut-off dimensional wavelength  $k_1 = \sqrt{\rho A_0/\alpha}$ . The fact that for the shorter wavelengths with  $k > k_1$ , the Rayleigh-Taylor instability is suppressed by the surface tension has already been established for plane liquid films accelerated by the pressure differential.<sup>4</sup>

The general characteristic equation (29) is readily solved numerically using, for example, the Jenkins-Traub method and all four its roots are explicitly found. For example, in the case of  $Re = We = 1000$ ,  $\gamma = 1.4$ ,  $P_2 = 0$  (vacuum outside),  $Q = 0.1$ , and  $s = 2$ , the four roots are

$$\begin{aligned} v_1 &= 0.881\,544\,71, & v_2 &= -0.899\,567\,43, \\ v_3 &= -0.000\,988\,63 + i0.893\,858\,08, & v_4 &= -0.000\,988\,63 - i0.893\,858\,08. \end{aligned} \tag{37}$$

It is seen that in full accordance with the general algebraic considerations based on Descartes’s rule of signs, there is only one real positive root  $v_1 = 0.881\,544\,71$ , and it determines the Rayleigh-Taylor instability right after the explosion in the present case. The entire calculated unstable part of the spectrum (29) is shown in Fig. 3. It is seen that the largest value of  $v \approx 2.53$  is reached at  $s \approx 31$ . This points out at the presence of the fastest growing mode of the perturbations which will be discussed in Sec. VIII.

### VIII. DEVELOPMENT OF THE RAYLEIGH-TAYLOR INSTABILITY. SMALL PERTURBATION GROWTH AT ARBITRARY TIME MOMENTS

At arbitrary time moments, the coefficients in Eqs. (22)–(24) determined by the unperturbed motion through Eqs. (20) and (21) depend on the dimensionless time  $\tau$ . Then, the solutions for the perturbations will not depend on  $\tau$  exponentially [as in the “frozen” case of Eq. (28) where only the increment  $v$  is to be found] anymore, but should be fully established. Then, instead of Eq. (28), the dimensionless perturbations are sought in the following form:

$$\chi = X(\tau) \exp(is\varphi), \quad \omega_1 = -iW_1(\tau) \exp(is\varphi), \quad \delta = D(\tau) \exp(is\varphi), \tag{38}$$

where the amplitude functions  $X(\tau)$ ,  $W_1(\tau)$ , and  $D(\tau)$  are to be found.

Substituting Eq. (38) into Eqs. (22)–(24), the ordinary differential equations describing  $X(\tau)$ ,  $W_1(\tau)$ , and  $D(\tau)$  are established. Combining these equations with Eqs. (20) and (21) for the unperturbed motion, we arrive at the following system of six ordinary differential equations to be solved

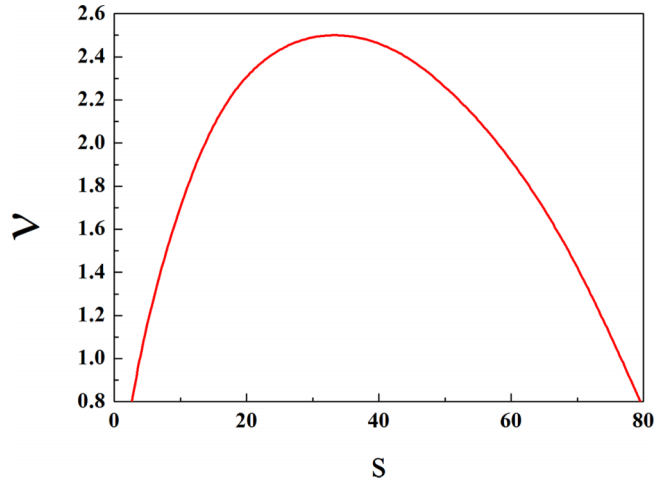


FIG. 3. The spectrum of the unstable growing perturbations in the case of  $Re = We = 1000$ ,  $\gamma = 1.4$ ,  $P_2 = 0$  (vacuum outside), and  $Q = 0.1$ . The line spans the values of  $\nu$  corresponding to several integer values of  $s$ .

numerically to find simultaneously the unperturbed motion and perturbations on top of it:

$$\frac{dr}{d\tau} = u, \quad (39)$$

$$\frac{du}{d\tau} = \frac{(\gamma - 1)}{r^{2\gamma-1}} - \frac{2P_2 r}{Q} - \frac{4}{Re} \frac{u}{r^2} - \frac{2}{rWe}, \quad (40)$$

$$\frac{dX}{d\tau} = -F - \frac{s}{r} W_1, \quad (41)$$

$$\begin{aligned} \frac{dW_1}{d\tau} = & -W_1 \frac{u}{r} + s a D - \frac{2}{Re} \frac{1}{r} \left( s F + \frac{W_1 s^2}{r} - s \frac{dX}{d\tau} \right) \\ & - \frac{4}{Re} \frac{u}{r^3} s X - \frac{Q^2}{8We} \frac{1}{r^4} [(2s^2 - s^3) X - 2(s - s^3) D], \end{aligned} \quad (42)$$

$$\frac{dD}{d\tau} = F, \quad (43)$$

$$\begin{aligned} \frac{dF}{d\tau} = & -\frac{2u}{r} F - 2\frac{a}{r} D - \frac{a}{r} X + \left[ \frac{(\gamma - 1)}{r^{2\gamma}} - \frac{2P_2}{Q} \right] D \\ & - \left( \frac{4}{Re} \frac{u}{r^3} + \frac{2}{We} \frac{1}{r^2} \right) s^2 D - \frac{4}{Re} \frac{u}{r^3} X - \frac{2}{Re} \frac{1}{r^2} \left( F + \frac{s}{r} W_1 - \frac{dX}{d\tau} \right). \end{aligned} \quad (44)$$

It should be emphasized that the auxiliary function  $F = dD/d\tau$  is introduced to split the second-order equation for  $d^2D/d\tau^2$  into two first-order equations for  $dD/d\tau$  and  $dF/d\tau$ . Note also, that since the solutions of the system (39)–(44) always pass through the initial stage, which was studied as the “frozen” case in Section VII, the values of  $s$  should be taken only from the unstable part of the spectrum  $\nu = \nu(s)$  of the characteristic equation (29). Then, the initial amplitudes of  $X$  and  $W_1$  should be related accordingly to the arbitrary bending amplitudes  $D_{0s}$  (different for different  $s$ , in the general case). Namely, the initial conditions for the system (39)–(44) are as follows: at  $\tau = 0$ :

$$r = 1, \quad u = 0, \quad (45)$$

$$X = X_0 = -D_{0s} \frac{[\nu^2 + Q^2 s^2 (1 - s)(3s + 2) / (8We) + s^2 a_0]}{[\nu^2 + 4s^2 \nu / Re - Q^2 (2 - s^2) s^2 / (8We)]}, \quad (46)$$

$$W_1 = W_{10} = D_{0s} \frac{sv [a_0 - 4v/\text{Re} + Q^2(4 - 3s^2)/(8\text{We})]}{[v^2 + 4s^2v/\text{Re} - Q^2(2 - s^2)s^2/(8\text{We})]}, \quad (47)$$

$$D = D_{0s}, \quad F = vD_{0s}. \quad (48)$$

Note that the values of  $v$  in the initial conditions (46) and (47) are found as the real positive solutions of the characteristic equation (29) for any  $s$  from the unstable band (36) to have the initial perturbations self-consistent. Namely, when Eqs. (27) and (28) are substituted into Eqs. (22)–(24), as usual in the linear stability analysis, a system of three homogeneous linear algebraic equations for the perturbation amplitudes  $\delta_0$ ,  $\chi_0$ , and  $\omega_{10}$  arises. It has non-trivial solutions only when its determinant is equal to zero, which means that the increment  $v$  satisfies the characteristic equation (29). Accordingly, two solutions can be expressed through the third one, namely,  $\chi_0$  and  $\omega_{10}$  are expressed through the initial perturbation amplitude  $\delta_0$ . These expressions form the initial conditions (45)–(48), where  $X_0$  and  $W_{10}$  play the role of  $\chi_0$  and  $\omega_{10}$ , while  $D_{0s}$  plays the role of  $\delta_0$  for any azimuthal wavenumber  $s$ . Then, the “unfrozen” fully transient case considered in the present section develops as a continuation of the “frozen” short-time case explored in Section VII. This also implies that the magnitudes of the initial amplitudes  $X_0$  and  $W_{10}$  can be rather high at larger  $s$ , resulting in a fast growth of not only the mode corresponding to the maximum of the spectrum  $v = v(s)$ , cf. Fig. 3.

The system of the ordinary differential equations (39)–(44) with the initial conditions (45)–(48) was solved using the Kutta-Merson method with the automatic variation of the time step according to the prescribed accuracy of four decimal digits. In the present case, the input parameters were chosen as in Section VII:  $\text{Re} = \text{We} = 1000$ ,  $\gamma = 1.4$ ,  $P_2 = 0$  (vacuum outside), and  $Q = 0.1$ , and 9 modes of perturbations with  $s = 2, 12, 21, 31, 41, 50, 60, 70$ , and  $80$  uniformly covering the unstable spectrum of the problem (see Fig. 3) were tracked. The shape of the perturbed centerline of the specimen during the perturbation growth was recovered as

$$R(\tau, \varphi) = r(\tau) \left[ 1 + \sum_{s=2}^N D_{0s} \cos(s\varphi) \right] \quad (49)$$

with the summation over the above-mentioned 9 modes with non-zero  $D_{0s}$  at  $\tau = 0$ . Their initial bending amplitudes were chosen as random numbers from the interval 0 to 0.001. The results will be presented using the Cartesian coordinates  $x$  and  $y$  in the parametric form

$$x(\tau, \varphi) = R(\tau, \varphi) \cos(s\varphi), \quad y(\tau, \varphi) = R(\tau, \varphi) \sin(s\varphi). \quad (50)$$

It should be emphasized that the superposition of the different modes in Eqs. (49) and (50) is possible, since perturbations are considered to be small and thus the problem is linear.

## IX. NUMERICAL AND ANALYTIC SOLUTIONS

The predicted evolution of the unperturbed radius of a specimen centerline is presented in Fig. 4 in the dimensionless form. It is seen that after the explosion at  $\tau = 0$ , the centerline rapidly expands under the action of high pressure of the explosion products in the cavity.

Simultaneously, the amplitudes of all 9 perturbation modes imposed at  $\tau = 0$  in the present calculations, namely, the bending amplitudes of the 9 centerline bending modes with non-zero  $D_{0s}$  at  $\tau = 0$  begin to grow. They are presented in Fig. 5 as functions of time. It should be emphasized that some modes grow faster than the other ones not only because their increments at the very beginning are close to the maximum of the spectrum in Fig. 3 but also because the corresponding initial amplitudes of the thickness perturbations  $X_0$  and the perturbation velocity component  $W_{10}$  determined by Eqs. (46) and (47) are higher for these modes. Therefore, the growth of the mode  $s = 80$ , which is well below the maximum in Fig. 3, is in fact, the fastest during the time period covered in Fig. 5. Note also, that the initial values  $D_{0s}$  are different and might be larger for the modes aside from the maximum of the spectrum  $v = v(s)$ .

The overall pattern of the evolution of the specimen centerline corresponding to these 9 modes triggered at the moment of explosion at  $\tau = 0$  is shown in Fig. 6. Note that perturbations grow on the

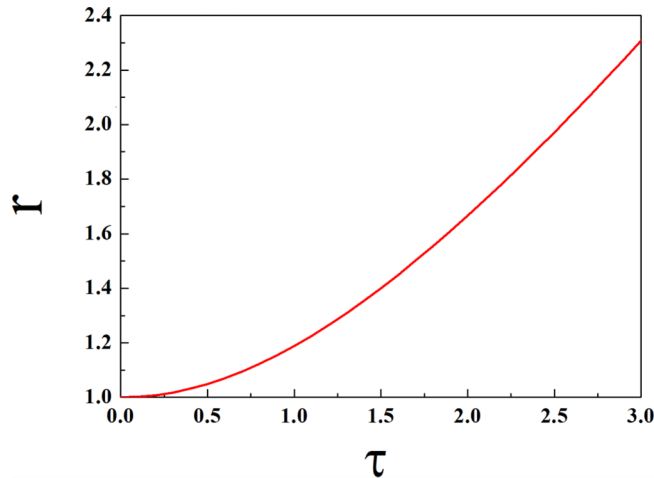


FIG. 4. Unperturbed radius of the centerline versus time.  $Re = We = 1000$ ,  $\gamma = 1.4$ ,  $P_2 = 0$  (vacuum outside), and  $Q = 0.1$ .

background of the rapidly expanding sample (also cf. with Fig. 4). Note also that the linear stability analysis implies that the perturbation amplitude is significantly smaller than the radius of the unperturbed centerline of liquid specimen [cf. Eq. (10)], which is not the case in Figs. 6(d)–6(f). However, even the latter cases stretched outside the formal range of validity of the linear analysis are quite instructive, since it is known, for example, that the linear Rayleigh-Weber theory is quite accurate in predicting the capillary breakup time, even though it misses some minor nonlinear morphological features (such as the satellite formation) which develop at the very end of the process.<sup>4</sup> Moreover, the fastest growing wavelengths and thus the number of the main fingers are inevitably predetermined by the linear stage, which means that the patterns depicted in Figs. 6(d)–6(f) are still quite plausible.

Figure 6 shows that as the specimen is expanding rapidly, the bending perturbations driven by the Rayleigh-Taylor instability resulting from the pressure differential between the inner and outer surfaces increase rapidly as well. This happens in spite of the fact that the pressure differential decreases as  $r^{-2\gamma}$  [cf. Eq. (6)] as the specimen expands (i.e.,  $r$  increases). For the rapid increase of the perturbation amplitudes, it is enough that the pressure differential stays positive. As a result of the Rayleigh-Taylor instability, the specimen practically breaks up at the moment  $\tau = 31$  (Fig. 6(f)) in the linear approximation. According to the results of Section VII, the fragment size is expected to be of the order of

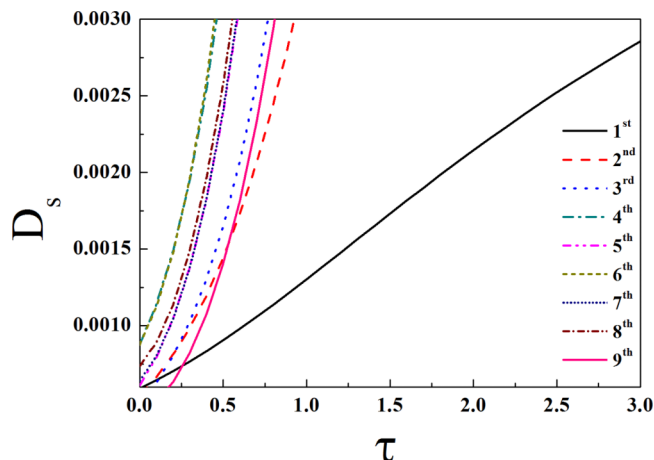


FIG. 5. Amplitudes of 9 modes of bending perturbations of the centerline versus time.  $Re = We = 1000$ ,  $\gamma = 1.4$ ,  $P_2 = 0$  (vacuum outside), and  $Q = 0.1$ . The initial bending amplitudes were chosen as random numbers from the interval 0 to 0.001.

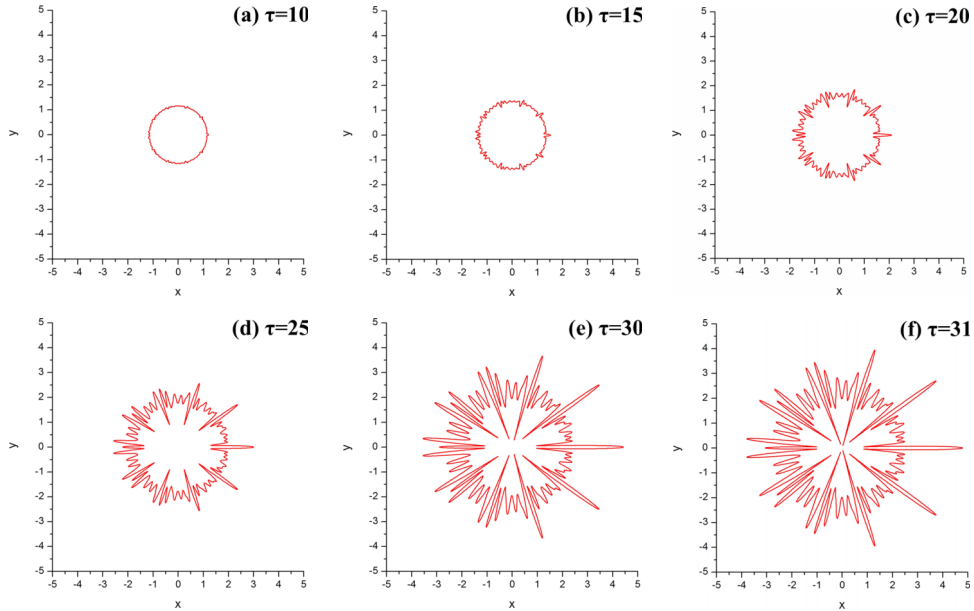


FIG. 6. Shape of the specimen centerline at different time moments: (a)  $\tau = 10$ ; (b)  $\tau = 15$ ; (c)  $\tau = 20$ ; (d)  $\tau = 25$ ; (e)  $\tau = 30$ ; (f)  $\tau = 31$ .  $Re = We = 1000$ ,  $\gamma = 1.4$ ,  $P_2 = 0$  (vacuum outside), and  $Q = 0.1$ . The initial bending amplitudes were chosen as random numbers from the interval 0 to 0.001.

$$\lambda = \frac{2\pi}{\sqrt{\rho A_0/\alpha}}, \quad (51)$$

where Eq. (9) yields the acceleration  $A_0$  as  $A_0 = \Delta P_0/\rho h_0 - \tau_0/\rho R_0 - 2\alpha/\rho h_0 R_0$ . At the explosion moment, the viscous and surface tension effects can be neglected, and thus  $A_0 \approx \Delta P_0/\rho h_0$ . Also, at the explosion moment  $t = 0$ , the pressure in the cavity is much higher than the atmospheric pressure, i.e.,  $P_{00}^+ \gg P_0^-$  and thus,  $\Delta P_0 \approx P_{00}^+$ . Therefore,

$$A_0|_{t=0} \approx \frac{P_{00}^+}{\rho H_0}. \quad (52)$$

Assuming that the gas in the cavity follows the equation of state of the ideal gas (any other equation can be used similarly), one obtains

$$P_{00}^+ \pi R_{00}^2 \times 1 = \frac{M}{\mu_a} R_g T_0 = \frac{M}{\mu_a} (c_p - c_v) T_0 = \frac{M}{\mu_a} c_v T_0 (\gamma - 1) = E (\gamma - 1), \quad (53)$$

where  $R_g$  is the absolute gas constant and  $c_p$  is the specific heat at constant pressure.

Finding from Eq. (53) that  $P_{00}^+ = E_1(\gamma - 1)/(\pi R_{00}^2)$ , one obtains from Eq. (52)

$$A_0|_{t=0} \approx \frac{E_1(\gamma - 1)}{\pi R_{00}^2 \rho H_0} \quad (54)$$

and, accordingly, from Eq. (51)

$$\lambda = 2\pi^{3/2} R_{00} \sqrt{\frac{\alpha H_0}{E_1(\gamma - 1)}}. \quad (55)$$

The latter expression shows that the debris size scales with the energy released by the explosive as  $\lambda \sim E^{-1/2}$  (obviously, the higher is the explosion energy, the smaller are the debris; however, the scaling  $-1/2$  is non-trivial). It also shows that the debris size is finite only when the surface tension is accounted for.

The debris size was estimated using the data acquired at eight different azimuthal locations. The largest size variation was observed between the 5th and 9th modes, with the difference of about 18%. Excluding the 5th mode, the difference remained within 9% relative to the 9th mode. Thus, it

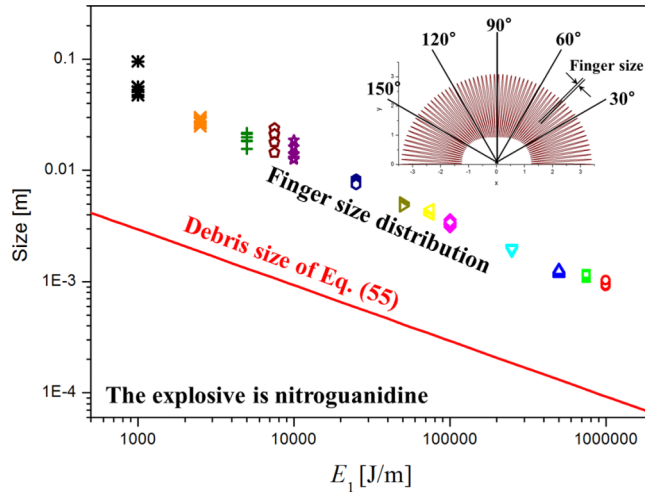


FIG. 7. Comparison of the analytic and numerical results for the debris size at different explosive energies  $E_1$ . It should be emphasized that Eq. (55) should be considered only as a scaling estimate, given the uncertainty in the finger size measurement shown in Figs. 12(e) and 12(f). Therefore, the comparison of the numerical solution with the results of Eq. (55) should be judged by the overall shape of the curve corresponding to the predicted dependence rather than by the absolute values.

was concluded that the debris size prediction was accurate up to 10% when the modes beyond the 9th mode are truncated.

Figure 7 compares the theoretical result based on Eq. (55) and the numerical solution based on Eqs. (39)–(44) and (49). The values of  $\lambda$  predicted by Eq. (55) are referred to as the “Debris size” and are compared to the “Finger size” depicted in the inset in Fig. 7 and predicted numerically. The explosive is assumed to be Nitroguanidine whose molar mass and density are 0.104 07 kg/mol and 1710 kg/m<sup>3</sup>, respectively. The liquid surrounding the explosive was assumed to be water whose density, surface tension, and viscosity are 1000 kg/m<sup>3</sup>, 0.0728 N/m, and 0.001 kg/m, respectively. The geometric dimensionless group  $Q$  was taken as  $Q = 3.28$ .

The finger size was estimated at five angular locations of 30°, 60°, 90°, 120° and 150° as depicted in the inset in Fig. 7. The explosive energy per unit core length  $E_1$  was varied in the 10<sup>3</sup>–10<sup>6</sup> J/m range.

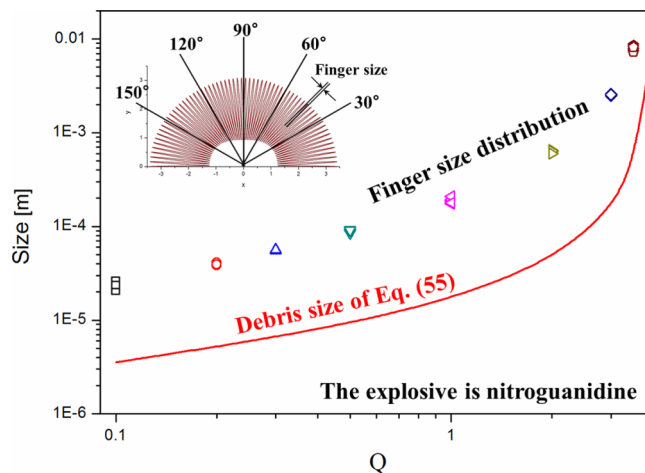


FIG. 8. Comparison of the analytic and numerical results for the debris size at varying dimensionless initial layer thickness  $Q$ . It should be emphasized that Eq. (55) should be considered only as a scaling estimate, given the uncertainty in finger size measurement shown in Figs. 12(e) and 12(f). Therefore, the comparison of the numerical solution with the results of Eq. (55) should be judged by the overall shape of the curve corresponding to the predicted dependence rather than by the absolute values.

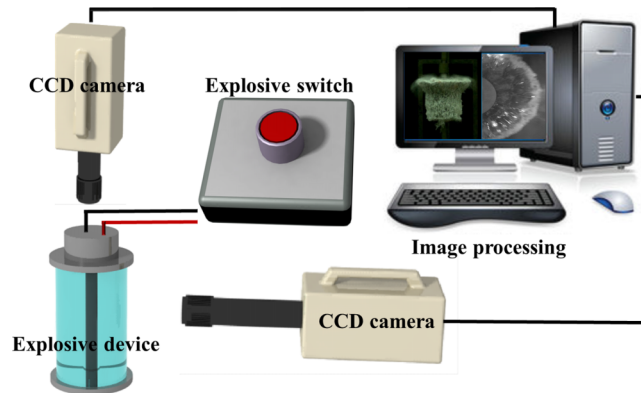


FIG. 9. Schematic of the explosive dispersion device.

Note that the absolute values of the “Debris sizes” and the “Finger sizes” differ by the factor of 10 since Eq. (55) is only an order-of-magnitude estimate. The scaling predicted by the analytic solution of Eq. (55) is in excellent agreement with the predictions of the numerical solution, as their practically identical slopes in the log-log plot in Fig. 7 show.

Figure 8 compares the predictions of Eq. (55) with the numerical results based on Eq. (49) at five different azimuthal locations versus the varying dimensionless initial liquid layer thickness  $Q$ . The explosive is assumed to be Nitroguanidine and the liquid is water. The explosive energy of 100 kJ is assumed.

As  $Q$  increases, the thickness of the liquid layer increases. Accordingly, both the finger and debris size increases. The overall agreement of the shape of the analytical and numerical dependences is quite satisfactory, as is seen in Fig. 8.

## X. EXPERIMENTAL RESULTS AND DISCUSSION

Figure 9 shows the schematic of the experimental setup. The high speed cameras were installed on top and side (Phantom v1211 and v7.3, respectively). The cameras’ frame speed was 10 000 fps with the time interval of 100  $\mu$ s. The image resolution was fixed at 1280  $\times$  800.

Figure 10 depicts in detail the explosive device used in the present experiments. The cylinder outer diameter and length were  $d = 134$  mm and  $L = 400$  mm, respectively. The cylinder

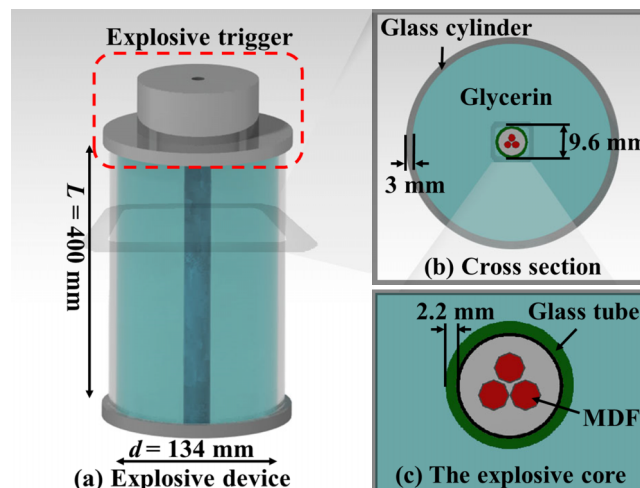


FIG. 10. The detailed construction of the explosive dispersion device. (a) The overall view. (b) The cross-sectional view. (c) The explosive core including the Mild Detonating Fuse (MDF).

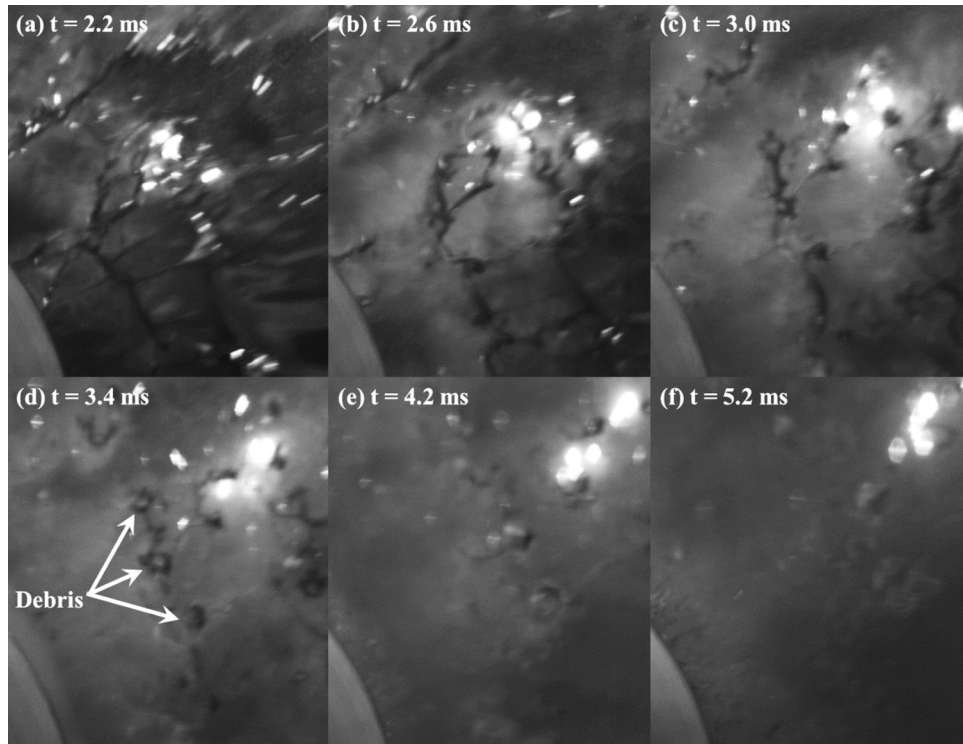


FIG. 11. Breakup droplets, originating from the expanding liquid shell and their evolution in time. The liquid shell is glycerin and the explosive is 3.4 g MDF.

top was connected to the explosion switch as shown in Fig. 9. The cross-sectional view of the cylinder is shown in Fig. 10(b). The exploding viscous Newtonian liquid, an almost pure glycerin, with density of  $1261 \text{ kg/m}^3$ , surface tension of  $0.064 \text{ N/m}$ , and viscosity of  $1.412 \text{ Pa s}$  was encased in the glass cylinder with the wall thickness of  $3 \text{ mm}$ . The glass encasing was of little effect on the explosion pattern as its fragility facilitated its quick disintegration upon explosion. In Fig. 10(c), the inner cylinder of  $9.6 \text{ mm}$  diameter includes the three explosive wires of Mild Detonating Fuse (MDF) whose density and specific heat release are  $1710 \text{ kg/m}^3$  and  $4\,968\,943 \text{ J/kg}$ , respectively.

### A. Breakup phenomenon

Ligaments are formed after the explosion of MDF and then they undergo the breakup process, as shown in Fig. 11. A few of the ligaments merge and then form droplets or “debris.” Therefore, the debris size tends to be larger than the thickness of the ligament originating from the expanding liquid shell. These breakup droplets are subjected to the aerodynamic drag, as well as to the convective heat transfer. The former causes the secondary breakup, while the latter causes evaporation. Both processes diminish the droplet sizes.

TABLE I. Experimental case studies used for comparison with the theoretical/numerical results.

Case	MDF mass (g)	Q	Re	We	The imaging time moment (ms)	$E_1$ (J/m)	E (J)
A1					1.1		
A2	1.4	3.90	$1.34 \times 10^3$	$2.56 \times 10^6$	1.4	17 391	6 956
A3					1.7		
B	3.4	3.85	$2.10 \times 10^3$	$6.18 \times 10^6$	1.4	42 236	16 894

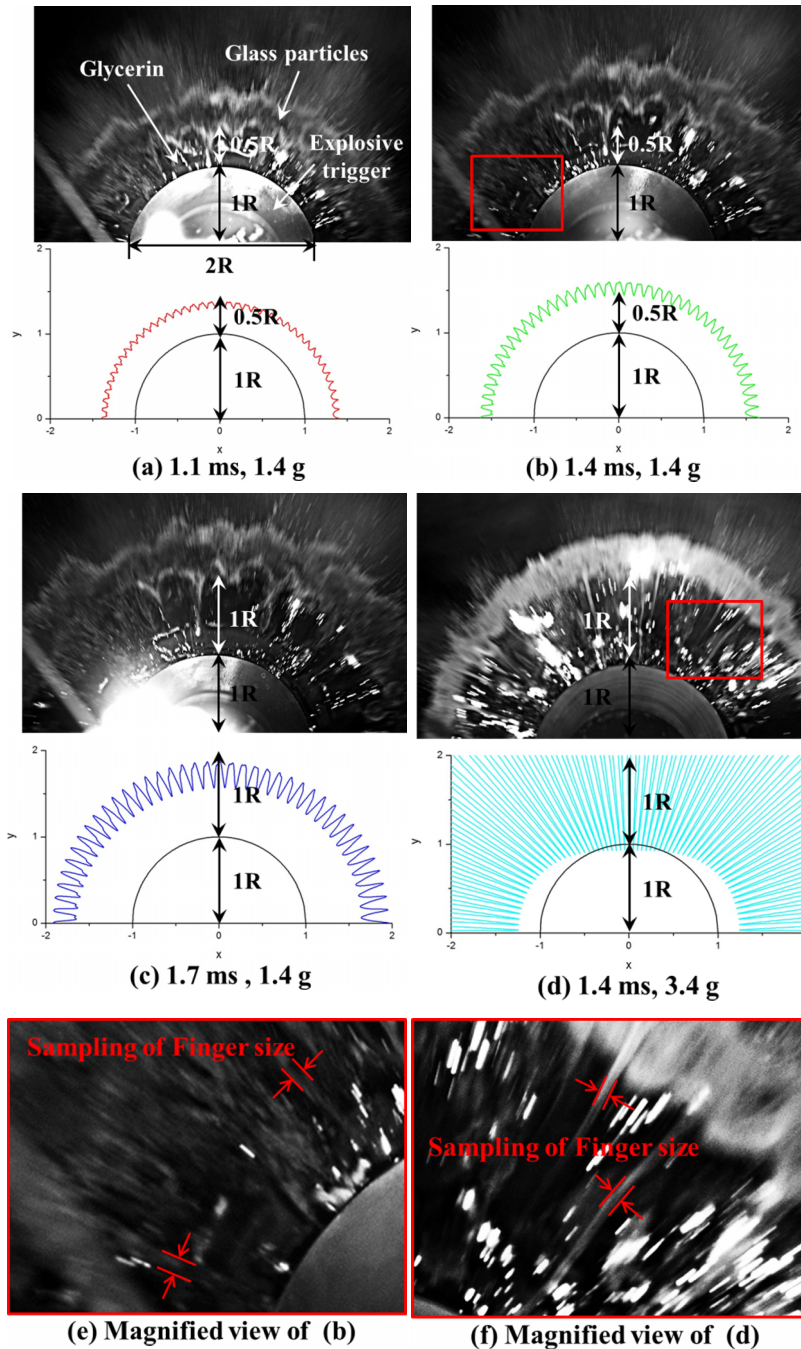


FIG. 12. (a)-(d) Experimental images (top views) compared with the numerical simulations (mode 9) for cases A1–A3 and B. The liquid shell is glycerin and the explosive is MDF. Here and hereinafter  $R$  denotes the outer radius of the glass cylindrical containers. (e) and (f) Magnified views which are used for sampling the finger sizes.

## B. Comparison between experiments and simulations

The experimental cases denoted in Table I as A1–A3 and B corresponded to the parameters listed in the table. These parameters correspond to the above-mentioned thermo-fluid properties of the materials (the viscous Newtonian liquid and the explosive). In cases A1–A3, the explosive MDF mass was the same, namely, 1.4 g, whereas the imaging time moments were different (see Table I). In case B, the MDF mass was larger than that in cases A1–A3, whereas the imaging time was the

same as in case A2. Accordingly, the debris size in case B is expected to be smaller than in cases A1–A3.

Figure 12 compares the experimental images with the numerical results obtained from Eqs. (39)–(44) and (49). The radially expanding liquid is seen in cases A1–A3, which correspond to their imaging time of  $t = 1.1, 1.4,$  and  $1.7$  ms at a given  $1.4$  g of MDF mass. The beginning of the explosion was set to  $t = 0$  ms. The Rayleigh-Taylor instability emerges because there is a pressure difference between the cavity and the surrounding atmosphere. The dimensionless unperturbed time was  $\tau = 1.45, 1.84, 2.23,$  and  $2.85$  for cases A1, A2, A3, and B, according to Eq. (25). Because the experiments were conducted in an open atmosphere,  $P_2 = 0.04$  and  $0.02$  for cases A and B, respectively. All of the experimental images were taken from the top of the cylinder, as described in Fig. 1.

Upon explosion of MDF, the outer glass shell is shattered into glass particles which are dispersed outward, followed by dispersion of glycerin. All dimensions are scaled by the cylinder radius denoted as  $R_{cr} = R_{00} + H_0/2$ . The perturbation amplitude growth is clearly revealed by the experimental images corresponding to cases A1–A3, as well as in the theoretical predictions. The simulation did not consider the outer glass shell, and nevertheless, the evolution of the perturbation wave exhibits significant similarity to the experimental observation, which implies that the effect of the glass shell is negligible. The latter observation is consistent with the dispersal phenomenon following the high-speed impact of liquid contained in a solid canister.<sup>22–24</sup>

When the mass of the explosive MDF increased from  $1.4$  g to  $3.4$  g (as in case B), explosive energy has in turn increased and therefore the liquid dispersal was intensified. The perturbation growth rate of the liquid surface is much faster and violent as the comparison between the cases A2 and B in Fig. 12 shows. It is noteworthy that the periphery of the outer shell appears rounder when the explosive mass was increased, cf. the photographs in Figs. 12(b) and 12(d). This appearance results from the smaller fragments of glass particles and liquid finger/droplets resulting from a stronger explosion, which is consistent with the consequences of the Rayleigh-Taylor instability, when higher acceleration results in smaller wavelength, as predicted in the present work (see also Refs. 25 and 26). The measurement of the finger sizes is shown in Figs. 12(e) and 12(f). An available resolution is unable to distinguish the smallest fingers which probably merge in these images, and this measurement overestimates the finger sizes, as is evident from Figs. 7 and 8.

It should be emphasized that both images (for cases A2 and B) were taken at the same time moment of  $t = 1.4$  ms, with all the other physical and geometrical parameters being the same, except a slight difference in  $Q$ . Thus the effect of the explosive mass is probed alone in comparison of A2 and B.

The surface undulation heights (effectively, the finger lengths) were measured in Fig. 12 and predicted numerically. The quantitative information resulting from such a comparison is presented in Table II, which shows the measured outermost radius normalized by the cylinder radius versus the predicted values. The agreement is good in all the cases.

Figure 13 compares the simulation results with the experimental data for the cases of  $1.4$  and  $3.4$  g explosives. The data in Fig. 13 correspond to those of Fig. 12 with a number of the intermediate snapshots (not shown there) being used. The case with the larger explosive mass of  $3.4$  g expanded faster in the experiments in agreement with the predictions. This observation is consistent with what was observed in the qualitative comparison shown in Fig. 12. The deviation of the numerical results from the experimental data increases in Fig. 13 at longer time because perturbations increase in amplitude, which makes radius measurements ambiguous.

TABLE II. Measured and predicted surface undulations.

		(a) 1.1 ms, 1.4 g	(b) 1.4 ms, 1.4 g	(c) 1.7 ms, 1.4 g	(d) 1.4 ms, 3.4 g
Prediction	$R/R_{cr}$	1.381	1.602	1.873	2.854
Experiment (error bar)		1.482 ( $\pm 0.077$ )	1.744 ( $\pm 0.101$ )	2.042 ( $\pm 0.160$ )	2.355 ( $\pm 0.198$ )

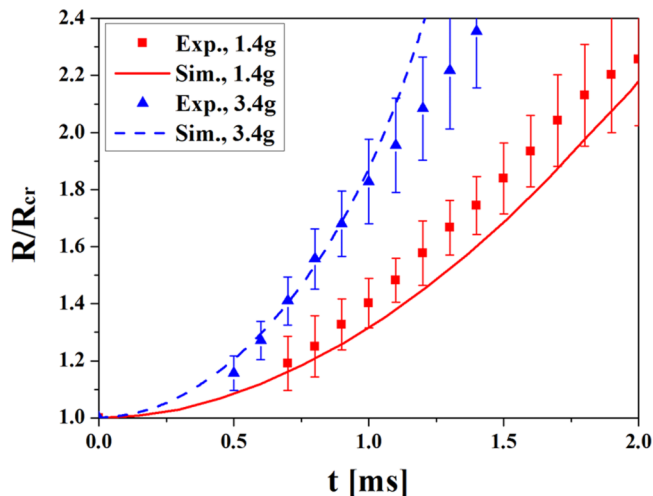


FIG. 13. Comparison of the experimental data with the predictions for the expanding shell radius.

Using Fig. 12, the number of fingers protruding from the expanding liquid shell in the experiment was estimated using the shape/geometry of the most obvious ones, such as those indicated by red arrows. Denoting the measured finger size in the azimuthal direction as  $\zeta_j$ , one can find the average value as  $\bar{\zeta} = (1/J) \sum_{j=1}^J \zeta_j$  where  $J$  is the sample size. Then, the number of the fingers as in Figs. 12(e) and 12(f) is estimated as  $N = 2\pi R_{cr}/\bar{\zeta}$ . Sampling was repeated 5 times and the average result was used. For the 1.4 g-explosive case, the number of fingers was found to be 73 at  $t = 1.4$  ms, while the numerically predicted number was 80 at  $t = 1.4$  ms, making the difference of about 9%. For the 3.4 g-explosive case, the numbers of fingers in the experiment and numerics were 118 and 126 (both at  $t = 1.4$  ms), respectively, with the difference of about 6%. The finger number does not seem to be changing in time during shell expansion in both the experimental and numerical results, since in the case of the 1.4-g explosive, it was 73 in the experiment at  $t = 1.1$  ms,  $t = 1.4$  ms and  $t = 1.7$  ms, and 80 according to the numerical predictions for the same three time moments.

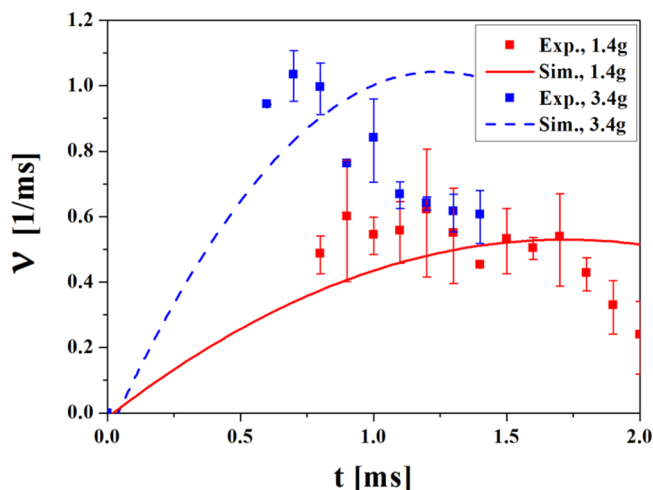


FIG. 14. The fastest perturbation growth rate versus time. The experimental data are shown by red and blue symbols and correspond to the cases listed in the inset. The corresponding numerical predictions are shown by lines with the corresponding colors.

If one assumes that the explosion energy is proportional to the explosive mass  $m_e$ , then the number of fingers  $N$  which follows from the scaling law of Eq. (55) is  $N \sim m_e^{1/2}$ . Then, one expects that  $N_2/N_1 = (m_{e2}/m_{e1})^{1/2}$ . In the experiments,  $m_1 = 1.4$  g,  $m_2 = 3.4$  g,  $N_1 = 73$ , and  $N_2 = 118$ . Accordingly,  $(m_{e2}/m_{e1})^{1/2} = 1.56$ , while  $N_2/N_1 = 1.62$ , which is pretty close to the expectation based on the scaling law. In the numerical predictions,  $N_1 = 126$  and  $N_2 = 80$ , which yields  $N_2/N_1 = 1.58$  in close agreement with the scaling law based on Eq. (55).

Figure 14 depicts the values of the perturbation growth rates found experimentally from the images in Fig. 12 (with a number of the intermediate images not shown there being used) and predicted numerically. Namely, the perturbation growth rate is determined as  $v = \ln \left[ (R/R_{cr})|_{t_2} / (R/R_{cr})|_{t_1} \right] / (t_2 - t_1)$ , where  $t_1$  and  $t_2$  are two consecutive time moments ( $t_2 > t_1$ ). The overall agreement of the predictions with the experimental data is quite satisfactory. The change in the perturbation growth rate in time stems from the time dependence of the basic flow, which has a stabilizing effect similarly to the case of the capillary breakup of thin liquid jets undergoing stretching.<sup>27</sup>

## XI. CONCLUSION

An explosion of an explosive material located in the core of a cylindrical liquid specimen will result in formation of a cavity filled with high-pressure gaseous products. The pressure differential between the inner and outer surfaces of the specimen accelerates the liquid layer toward the outside low-pressure atmosphere or vacuum. This triggers the special non-trivial case of the Rayleigh-Taylor instability of the specimen, and in particular, the growth of bending perturbations of its centerline. The linearized stability problem posed and solved in this work predicts the perturbation growth rates, the evolution of the sample shape, and the debris size resulting from the explosion. It is shown that the parameter most important practically, the debris size  $\lambda$ , scales with the energy  $E$  released by the explosive in the specimen core as  $\lambda \sim E^{-1/2}$ . This theoretical scaling law corresponding to Eq. (55) was in good agreement with the numerical results for a wide range of shell thicknesses and explosive energies.

The experimental results revealed that the outmost radius of the expanding liquid shell reached the distance of about  $1.5R$ – $2.2R$  (with  $R$  being the initial radius) in 2 ms after the explosion of 1.4 g of MDF. Another important parameter, the number of fingers, measured experimentally was within 6%–9% from the numerical predictions, and it practically did not change during the observation time in the experiments and predictions. The number of fingers  $N$  in the experiments and numerical predictions was in close agreement with the scaling law predicted theoretically, namely,  $N \sim m_e^{1/2}$ , where  $m_e$  is the mass of the explosive. Also, the predicted and measured perturbation growth rates were reasonably close to each other.

## ACKNOWLEDGMENTS

This research was mainly supported by Agency for Defense Development (Contract No. UD140051GD). This research was also supported by COMPA funded by the Ministry of Science, ICT and Future Planning (MSIP). S. S. Yoon extends his appreciation to the Vice Deanship of Scientific Research Chairs at King Saud University.

<sup>1</sup> V. M. Entov, F. M. Sultanov, and A. L. Yarin, "Breakup of liquid films under the action of a pressure drop in the ambient gas," *Sov. Phys.-Dokl.* **30**, 882–884 (1985).

<sup>2</sup> S. V. Stebnovskii, "The growth of initial perturbations at the outer boundary of an expanding gas-liquid ring," *J. Appl. Mech. Tech. Phys.* **23**, 45–50 (1982).

<sup>3</sup> S. V. Stebnovskii and N. N. Chernobaev, "Energy threshold for impulsive failure of a liquid volume," *J. Appl. Mech. Tech. Phys.* **27**, 51–54 (1986).

<sup>4</sup> A. L. Yarin, *Free Liquid Jets and Films: Hydrodynamics and Rheology* (Longman Scientific & Technical and John Wiley & Sons, Harlow, New York, 1993).

<sup>5</sup> D. L. Frost, Y. Grégoire, O. Petel, S. Goroshin, and F. Zhang, "Particle jet formation during explosive dispersal of solid particles," *Phys. Fluids* **24**, 091109 (2012).

<sup>6</sup> S. Hall and G. Knowlton, "Development, characterization and testing of high blast thermobaric compositions," in *Proceedings International Pyrotechnics Seminar*, Fort Collins, CO, 11–16 July 2004.

- <sup>7</sup> D. R. Gardner, *Near-Field Dispersal Modeling for Liquid Fuel-Air Explosives* (Sandia National Laboratories, Albuquerque, NM, USA, 1990).
- <sup>8</sup> S. Singh and V. Singh, "Extended near field modelling and droplet size distribution for fuel air explosive warhead," *Def. Sci. J.* **51**, 303–314 (2002).
- <sup>9</sup> X. X. Lu, L. Li, X. B. Ren, X. F. Yan, and Y. C. Dong, "Numerical simulations of interactions between shock wave and gas-liquid-air interfaces," *J. Phys.: Conf. Ser.* **216**, 012012 (2010).
- <sup>10</sup> O. B. Kudryashova, B. I. Vorozhtsov, E. V. Muravlev, I. R. Akhmadeev, A. A. Pavlenko, and S. S. Titov, "Physico-mathematical modeling of explosive dispersion of liquid and powders," *Propellants, Explos., Pyrotech.* **36**, 524–530 (2011).
- <sup>11</sup> R. J. Zabelka and L. H. Smith, *Explosively Dispersed Liquids. Part 1. Dispersion Model* (DTIC, 1969).
- <sup>12</sup> M. Samirant, "Dispersion-initiation and detonation of liquid and dust aerosols-experiences derived from military fuel-air explosives," in *Prevention of Hazardous Fires and Explosions* (Springer, Netherlands, 1999), pp. 123–134.
- <sup>13</sup> L. Li, X. Ren, X. Lu, and X. Yan, "On the characteristics of liquid explosive dispersing flow," *World Acad. Sci. Eng. Technol.* **4**, 526–530 (2010).
- <sup>14</sup> F. Zhang, R. C. Ripley, A. Yoshinaka, C. R. Findlay, J. Anderson, and B. von Rosen, "Large-scale spray detonation and related particle jetting instability phenomenon," *Shock Waves* **25**, 239–254 (2015).
- <sup>15</sup> L. I. Sedov, "Propagation of strong blast waves," *J. Appl. Math. Mech.* **10**, 241–250 (1946).
- <sup>16</sup> L. I. Sedov, *Similarity and Dimensional Methods in Mechanics* (CRC Press, Boca Raton, 1993).
- <sup>17</sup> G. Taylor, "The formation of a blast wave by a very intense explosion. I. Theoretical discussion," *Proc. R. Soc. London, Ser. A* **201**, 159–174 (1950).
- <sup>18</sup> G. Taylor, "The formation of a blast wave by a very intense explosion. II. The atomic explosion of 1945," *Proc. R. Soc. London, Ser. A* **201**, 175–186 (1950).
- <sup>19</sup> J. von Neumann, *The Point Source Solution*, Collected Works (Pergamon Press, New York, 1963), Vol. VI.
- <sup>20</sup> J. Liu, *Liquid Explosives* (Springer, Berlin, 2015).
- <sup>21</sup> B. E. Meserve, *Fundamental Concepts of Algebra* (Dover Publications, New York, 1982).
- <sup>22</sup> S. Hostikka, A. Silde, T. Sikanen, A. Vepsä, A. Paajanen, and M. Honkanen, "Experimental characterisation of sprays resulting from impacts of liquid-containing projectiles," *Nucl. Eng. Des.* **295**, 388–402 (2015).
- <sup>23</sup> R. A. Jepsen, T. O'Hern, B. Demosthenous, E. Bystrom, M. Nissen, E. Romero, and S. S. Yoon, "Diagnostics for liquid dispersion due to a high-speed impact with accident or vulnerability assessment application," *Meas. Sci. Technol.* **20**, 025401 (2008).
- <sup>24</sup> A. Silde, S. Hostikka, and A. Kankkunen, "Experimental and numerical studies of liquid dispersal from a soft projectile impacting a wall," *Nucl. Eng. Des.* **241**, 617–624 (2011).
- <sup>25</sup> I. Bernstein and D. Book, "Rayleigh-Taylor instability of a self-similar spherical expansion," *Astrophys. J.* **225**, 633–640 (1978).
- <sup>26</sup> S. Hwang, Z. Liu, and R. D. Reitz, "Breakup mechanisms and drag coefficients of high-speed vaporizing liquid drops," *Atomization Sprays* **6**, 353–376 (1996).
- <sup>27</sup> A. Kolbasov, S. Sinha-Ray, A. Jojjode, M. A. Hassan, D. Brown, B. Maze, B. Pourdeyhimi, and A. L. Yarin, "Industrial-scale solution blowing of soy protein nanofibers," *Ind. Eng. Chem. Res.* **55**, 323–333 (2016).